Interferometric Monitoring of Gamma-Ray Bright AGNs: OJ 287

Jee Won Lee[1] , Sang-Sung Lee[1,2] , Juan-Carlos Algaba[3] , Jeffrey Hodgson[1,4] , Jae-Young Kim[5] , Jongho Park[6] ,
Motoki Kino[7,8] , Dae-Won Kim[9] , Sincheol Kang[1,2] , Sungmin Yoo[10] , Sang Hyun Kim[1,2] , and Mark Gurwell[11]

[1] Korea Astronomy and Space Science Institute, 776 Daedeok-daero, Yuseong-gu, Daejeon 34055, Republic of Korea; jwlee78@kasi.re.kr
[2] University of Science and Technology, 217 Gajeong-ro, Yuseong-gu, Daejeon 34113, Republic of Korea
[3] Department of Physics, Faculty of Science, University of Malaya, 50603 Kuala Lumpur, Malaysia
[4] Department of Physics and Astronomy, Sejong University, 209 Neungdong-ro, Gwangjin-gu, Seoul, Republic of Korea
[5] Max-Planck-Institut für Radioastronomie, Auf dem Hügel 69, D-53121 Bonn, Germany
[6] Institute of Astronomy and Astrophysics, Academia Sinica, P.O. Box 23-141, Taipei 10617, Taiwan
[7] National Astronomical Observatory of Japan, 2-21-1 Osawa, Mitaka, Tokyo 181-8588, Japan
[8] Kogakuin University of Technology & Engineering, Academic Support Center, 2665-1 Nakano, Hachioji, Tokyo 192-0015, Japan
[9] Department of Physics and Astronomy, Seoul National University, Gwanak-gu, Seoul 08826, Republic of Korea
[10] Department of Astronomy and Space Science, Chungbuk National University, Cheongju, 28644, Republic of Korea
[11] Center for Astrophysics, Harvard & Smithsonian, 60 Garden Street, Cambridge, MA 02138, USA
Received 2020 July 21; revised 2020 August 31; accepted 2020 August 31; published 2020 October 16

Abstract

We present the results of simultaneous multifrequency imaging observations at 22, 43, 86, and 129 GHz of OJ 287. We used the Korean Very Long Baseline Interferometry Network as part of the Interferometric Monitoring of Gamma-ray Bright active galactic nuclei (iMOGABA). The iMOGABA observations were performed during 31 epochs from 2013 January 16 to 2016 December 28. We also used 15 GHz OVRO and 225 GHz SMA flux density data. We analyzed four flux enhancements in the light curves. The estimated timescales of three flux enhancements were similar with timescales of ∼50 days at two frequencies. A fourth flux enhancement had a variability timescale approximately twice as long. We found that 225 GHz enhancements led the 15 GHz enhancements by a range of 7–30 days in the time delay analysis. We found the fractional variability did not change with frequency between 43 and 86 GHz. We could reliably measure the turnover frequency, ν_c, of the core of the source in three epochs. This was measured to be in a range from 27 to 50 GHz and a flux density at the turnover frequency, S_m, ranging from 3 to 6 Jy. The derived SSA magnetic fields, B_{SSA}, are in a range from 0.157 ± 0.104 to 0.255 ± 0.146 mG. We estimated the equipartition magnetic field strengths to be in a range from 0.95 ± 0.15 to 1.93 ± 0.30 mG. The equipartition magnetic field strengths are up to a factor of 10 higher than the values of B_{SSA}. We conclude that the downstream jet may be more particle energy dominated.

Supporting material: machine-readable tables

1. Introduction

Blazars are a subclass of radio-loud active galactic nuclei (AGN) which have a relativistic jet oriented toward the observer's line of sight. Blazars typically have a small viewing angle of <20° (Angel & Stockman 1980; Urry & Padovani 1995). The high Doppler factors associated with these small viewing angles shortens the observed flux density variation timescales and increases the brightness of observed flux densities. This variability as well as polarized emission has been observed on various timescales from days to years across the whole electromagnetic spectrum (Rani et al. 2013; Lee et al. 2016a, 2016b, 2017a, 2017b; Algaba et al. 2018a).

Simultaneous multifrequency Very Long Baseline Interferometry (VLBI) observations allow us to better understand the relativistic jets of AGN that emit synchrotron radiation. It enables us to investigate magnetic field strength, which is known to play an important role in jet formation, acceleration, and collimation (Begelman et al. 1984). We can do this by measuring the turnover frequency and the flux density, and the size of the source at the turnover frequency (Rybicki & Lightman 1986). In previous studies using the Interferometric Monitoring of Gamma-ray Bright AGN (iMOGABA) program (Lee et al. 2013, 2016b, 2017a; Algaba et al. 2018a, 2018b; Kim et al. 2018; Park et al. 2019), which is a part of the Korean

VLBI Network (KVN) key science programs, magnetic field strengths of a few mG were found in the SSA regions of the relativistic jets in S5 0716+714 (Lee et al. 2017a) and 1633 +382 (Algaba et al. 2018a).

OJ 287 is a well-known BL Lacertae-type blazar with a redshift $z = 0.306$ (Sitko & Junkkarinen 1985; Nilsson et al. 2010). Quasi-periodic flares with a period of 12 yr at optical wavelengths have been detected (Villforth et al. 2010). This is thought to be caused by a binary supermassive black hole system where a secondary black hole penetrates the accretion disk of the primary system (Sillanpaa et al. 1988). If OJ 287 is modeled as such a binary system, a black hole mass of $1.8 \times 10^{10} M_\odot$ can be derived for the primary black hole (Valtonen et al. 2008). Valtonen & Pihajoki (2013) suggested helical jet models to explain the source variability at optical and radio bands. Myserlis et al. (2018) introduced a helical jet model where a polarized emission component is propagating on a helical trajectory within a bent jet, for explaining the flux density and polarization variability at radio and optical bands. This can be used to explain the flux density variability. Britzen et al. (2018) interpreted the flux density variation at radio bands in OJ 287 within the context of a jet precession model finding a period of ∼22 yr. Valtonen et al. (2006) also applied the jet precession model to interpret the source variability.

VLBI observations have been conducted to study the milliarcsecond (mas) scale structures in the central regions of OJ 287, including the bright core with a one-sided jet in Very Long Baseline Array (VLBA) images at 43 GHz (Agudo et al. 2011). A quasi-stationary feature within 2 mas of the core associated with a bent jet, was analyzed using Global mm-VLBI Array (GMVA) observations at 86 GHz (Hodgson et al. 2017). The spectral index showed different behavior between the core and stationary component at millimeter wavelengths. The spectral index of the core at 15–43 GHz and 43–86 GHz was inverted. When the core was flaring, the spectral index changed to become steep (Hodgson et al. 2017).

In this paper, we report results from simultaneous multiple frequency VLBI observations of OJ 287 using the KVN at 22, 43, 86, and 129 GHz, from 2013 January until 2016 December. The paper is organized as follows. In Section 2, we present the description of the observations for both the KVN data and all archival data used in this paper. Sections 3 and 4 describe results and various analyses of the flux density variability at multiple frequencies, respectively, and Section 5 includes a discussion on the results and analysis. Finally, we summarize this paper in Section 6. We use luminosity distance $D_L = 1630$ Mpc at a redshift of $z = 0.306$, assuming $H_\circ = 68$ km s^{-1} Mpc^{-1}, $\Omega_\lambda = 0.698$, and $\Omega_m = 0.302$ (Spergel et al. 2015; Hodgson et al. 2016). Spectral index α is defined as $S_\nu \propto \nu^\alpha$.

2. Observations and Data Reduction

2.1. KVN Observations

OJ 287 was observed by the KVN, which is a 500 km scale VLBI network consisting of three 21 m radio telescopes located in Seoul (KVN Yonsei), Ulsan (KVN Ulsan), and Jeju (KVN Tamna), Korea. The observations were conducted at 22, 43, 86, and 129 GHz bands simultaneously with a mean cadence of roughly a month since 2012 December except for maintenance seasons from June to August.

The angular resolution of the KVN is 6 mas at 22 GHz, 3 mas at 43 GHz, 1.5 mas at 86 GHz, and 1 mas at 129 GHz. We used data obtained in 31 epochs in the period from 2013 January 16 (MJD 56308) until 2016 December 28 (MJD 57750). In each epoch, the source was observed with up to eight 5 minute scans per 24 hr. The observations were recorded in left circular polarization mode at a recording rate of 1 Gbps. The observing frequencies are 21.700–21.764, 43.400–43.464, 86.800–86.864, and 129.300–129.364 GHz, with a total bandwidth of 256 MHz (thus 64 MHz in each band). Detailed descriptions of the iMOGABA observations are reported in Lee et al. (2016b, 2017a).

2.2. Data Calibration

The obtained data were processed with the DiFX software correlator in Daejeon, Korea (Deller et al. 2007, 2011), and the data was calibrated following the standard procedures (phase and amplitude calibration, fringe fitting, and bandpass correction) in the AIPS package from the National Radio Astronomy Observatory (NRAO). For the calibration, the KVN pipeline was used (Hodgson et al. 2016).

The visibility phases in the 22 GHz band were transferred to those in the higher frequency bands (i.e., 43, 86, and 129 GHz bands) using the pipeline in order to increase the coherence time at the higher frequency bands and hence to improve the detection

sensitivity (Algaba et al. 2015). An amplitude requantization loss from the digital filter was corrected by applying a factor of 1.1 to the visibility amplitude of each station (Lee et al. 2015). The uncertainty of the amplitude calibration is expected to be 5% at 22 and 43 GHz, 10% at 86, and 30% at 129 GHz.

2.3. Imaging and Model-fitting

After data calibration in AIPS, the KVN data were imported into the Difmap software package for imaging in the same manner as described in Lee et al. (2017a).

The visibility data were averaged in time at 30 s intervals at 22, 43, and 86 GHz and 10 s intervals at 129 GHz, which are the typical coherence timescales of KVN observations.

We obtained a total of 106 VLBI images of OJ 287 at four frequencies during 31 epochs over four years. These include 31 images at 22 GHz, 27 images at 43 GHz, 26 images at 86 GHz, and 22 images at 129 GHz. We excluded data from several epochs at certain frequencies when the observations clearly suffered from large pointing errors or bad weather. The imaging process started with self-calibrating the visibility data based on a point-source model of 1 Jy (i.e., the STARTMOD task in Difmap). The CLEANing was performed until the residuals reached a certain total flux level, and then CLEAN was repeated with loops of phase self-calibration. The standard CLEANing and self-calibration within the central emission regions have been conducted until no significant flux density was added compared to the image rms level. Since OJ 287 is very compact on mas-scales with the KVN observations, the best CLEAN models to the data can be found quickly.

Figure 1 presents representative CLEAN contour maps of OJ 287 observed at 22 (top left), 43 (top right), 86 (bottom left), and 129 GHz (bottom right). The source has a compact structure on mas-scales at all observing frequencies with the KVN. In order to evaluate the image quality, we computed the image quality factor. This is the ratio of the image rms noise and its mathematical expectation, $\xi_r = S_r/S_{r,exp}$, where S_r is the maximum absolute flux density in the residual image and $S_{r,exp}$ is the expectation of S_r. For more detailed descriptions of this image quality evaluation scheme (see, Lobanov et al. 2006; Lee et al. 2016b, 2017a). ξ_r obtained in this paper is 0.42–0.89, which indicates that images sufficiently represent the structure detected in the visibility data although the image model with $\xi_r < 1$ has a large number of degrees of freedom.

We conducted model-fitting procedures in order to parameterize physical parameters such as size, flux density, locations, etc. When the fitted component size is smaller than minimum resolvable size according to Lee et al. (2016b), the component is considered to be unresolved. The minimum resolvable size was estimated for the core component to determine the upper limit following Lobanov (2005). The visibility data have been fitted with circular two-dimensional Gaussian components using the MODELFIT task in Difmap. If available, additional Gaussian components have been added until the χ^2 value of the fitting is no longer improved.

The brightness temperature T_b was estimated as $T_b = \frac{2\ln 2}{\pi k} \frac{S_{tot}\lambda^2}{d^2}(1 + z)$, where λ is the wavelength of the observation, z is the redshift, d is the fitted core size, and k is the Boltzmann constant. Table 1 lists the fitted parameters of the contour maps presented in Figure 1, including the observing frequencies, restoring beam size $B_{maj,min}$, position angle B_{PA}, total CLEANed flux density S_{KVN}, peak flux density S_p in units of Jy per beam, rms in the image σ, the dynamic range (ratio of
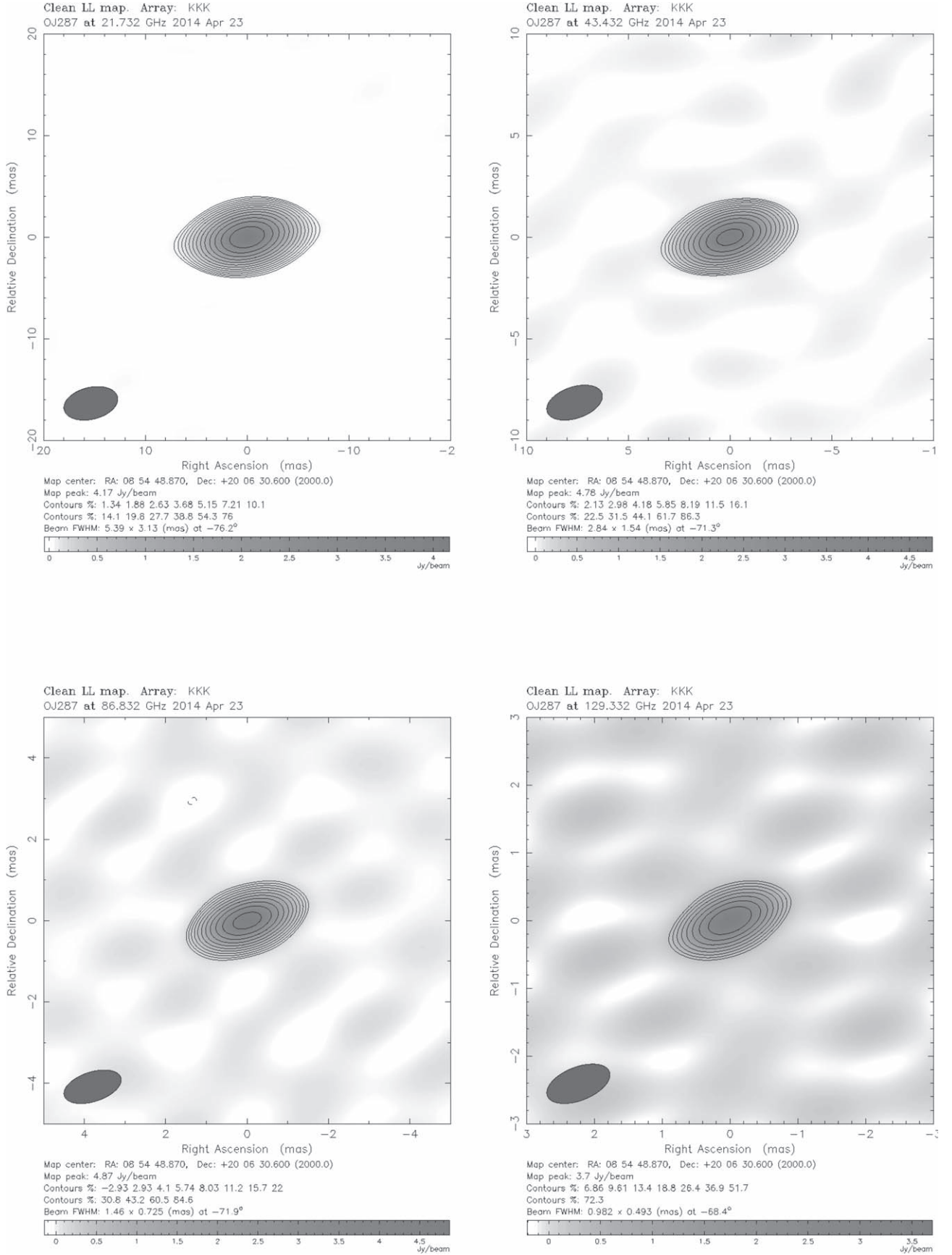
Figure 1. The CLEAN maps of OJ 287 obtained in Epoch 14 (2014 April 23), showing compact core-dominated structure at all frequencies from 22 to 129 GHz. In each panel, the contours start from three times the rms noise level and increase by factors of 2. Top left indicates 22 GHz, top right 43 GHz, bottom left 86 GHz, and bottom right 129 GHz.

Table 1
Image Parameters

Epoch (1)	MJD (2)	Band (3)	B_{maj} (4)	B_{min} (5)	B_{PA} (6)	S_{KVN} (7)	S_p (8)	σ (9)	D (10)	ξ_r (11)
2013 Jan 16	56308	K	5.396	3.234	−81.8	3.495	3.416	22	155	0.64
		Q	2.715	1.603	−80.0	3.792	3.616	26	141	0.71
		W	1.365	0.765	−69.7	2.692	2.712	45	60	0.60
		D	1.388	0.764	−69.6	2.520	2.599	75	35	0.55
2013 Mar 28	56379	K	9.785	3.131	−45.6	5.566	5.579	24	237	0.46
		D	1.610	0.498	−50.4	2.320	2.529	363	7	0.42
2013 Apr 11	56393	K	5.616	3.161	−77.7	5.095	4.963	17	291	0.61
		Q	2.765	1.523	−79.6	4.525	4.238	17	255	0.55
		W	1.556	0.708	−66.8	3.614	2.555	59	44	0.60
		D	1.013	0.502	−64.8	2.874	1.594	64	25	0.60
2013 May 7	56419	K	5.344	3.245	−78.3	4.029	3.980	10	407	0.60
		Q	2.641	1.728	−80.6	3.385	3.237	15	210	0.67
		W	1.377	0.753	−75.3	2.686	2.401	31	77	0.59
		D	0.920	0.513	−71.0	2.047	1.852	37	50	0.68
2013 Sep 24	56559	K	7.611	2.996	−55.4	4.189	4.048	24	168	0.60
		Q	2.912	1.547	−64.7	2.867	2.865	33	88	0.67
2013 Oct 15	56580	K	6.199	3.720	71.2	4.071	3.841	13	296	0.62
		Q	2.893	1.836	80.1	3.323	2.968	42	71	0.66
		W	1.447	0.781	82.0	2.602	2.442	38	64	0.63
		D	1.459	0.801	84.4	2.633	2.459	36	68	0.60
2013 Nov 19	56615	K	6.286	3.074	−65.7	4.703	4.688	43	109	0.61
		Q	3.233	1.497	−67.7	3.873	3.693	17	217	0.60
		W	1.784	0.698	−62.9	2.863	2.615	18	145	0.66
		D	1.062	0.520	−55.5	1.925	1.803	22	82	0.57
2013 Dec 24	56650	K	5.366	3.079	−79.7	3.181	3.086	11	282	0.77
		Q	2.612	1.600	−79.7	2.501	2.414	13	191	0.87
		W	1.397	0.712	−80.1	1.898	1.812	15	124	0.77
		D	1.021	0.442	−75.6	1.362	1.340	25	54	0.63
2014 Jan 27	56684	K	5.782	3.049	−68.8	2.765	2.761	16	172	0.72
		Q	2.747	1.602	−68.0	2.325	2.289	18	128	0.71
2014 Feb 28	56716	K	6.034	2.871	−66.6	3.110	2.971	13	232	0.47
		Q	3.039	1.434	−65.9	2.861	2.644	8	334	0.67
		W	2.097	0.605	−72.1	2.223	2.119	14	155	0.60
		D	1.481	0.402	−71.5	1.766	1.619	31	52	0.53
2014 Mar 22	56738	K	5.515	3.089	−68.4	2.851	2.776	9	324	0.76
		Q	2.745	1.562	−66.4	2.773	2.687	15	175	0.72
		W	1.495	0.718	−69.7	2.551	2.478	17	148	0.66
		D	1.016	0.484	−67.2	1.807	1.659	67	25	0.66
2014 Apr 22	56769	K	5.388	3.131	−76.2	4.278	4.171	19	224	0.57
		Q	2.838	1.544	−71.3	4.877	4.778	34	141	0.62
		W	1.461	0.725	−71.9	4.997	4.874	48	103	0.64
		D	0.982	0.493	−68.4	3.793	3.700	85	44	0.68
2014 Sep 1	56902	K	5.399	3.250	−80.4	4.843	4.743	18	267	0.68
		Q	2.892	1.531	−74.6	4.465	4.261	22	196	0.69
		W	1.408	0.731	−79.1	3.477	3.357	37	90	0.66
		D	1.408	0.735	−76.7	3.536	3.394	35	98	0.63
2014 Oct 29	56960	K	5.307	3.220	−79.2	5.731	5.535	18	303	0.89
		Q	2.636	1.691	−85.0	5.023	4.679	22	211	0.60
		W	1.464	0.659	−79.6	3.317	3.138	41	77	0.58
		D	1.564	0.493	58.4	1.387	1.352	72	19	0.44
2014 Nov 28	56990	K	5.717	2.847	−81.7	5.028	5.021	51	99	0.76
		Q	2.809	1.467	−82.5	4.485	4.433	43	104	0.58
		W	1.527	0.676	−73.7	3.493	3.351	43	78	0.65
2014 Dec 25	57017	K	5.503	3.005	−77.4	5.668	5.620	23	249	0.65
2015 Feb 23	57076	K	5.331	3.149	−81.2	7.144	7.089	15	464	0.57
		Q	2.661	1.584	−78.0	5.825	5.746	13	456	0.61
		W	1.419	0.732	−77.6	4.389	4.278	19	229	0.73
		D	0.934	0.492	−83.5	3.291	1.414	22	64	0.64
2015 Mar 26	57107	K	5.534	3.030	−74.1	5.162	5.065	11	470	0.70
		Q	2.804	1.517	−73.3	4.703	4.624	11	429	0.70
		W	1.465	0.721	−73.0	4.189	3.963	34	118	0.64
		D	0.956	0.507	−72.7	3.348	3.059	43	71	0.61
2015 Apr 30	57142	K	5.412	3.119	83.8	4.958	4.895	42	118	0.80

Table 1
(Continued)

Epoch (1)	MJD (2)	Band (3)	B_{maj} (4)	B_{min} (5)	B_{PA} (6)	S_{KVN} (7)	S_p (8)	σ (9)	D (10)	ξ_r (11)
		W	1.518	0.708	82.7	3.483	3.261	35	93	0.64
		D	1.001	0.465	−88.9	2.464	2.511	49	51	0.68
2015 Sep 24	57289	K	5.280	3.103	−84.8	3.377	3.344	25	133	0.88
		Q	2.659	1.480	−84.7	2.472	2.452	24	104	0.67
		W	1.458	0.701	86.8	1.831	1.753	27	65	0.60
2015 Oct 23	57318	K	5.660	3.079	−89.2	2.578	2.468	15	166	0.66
		Q	2.879	1.489	−87.2	2.267	2.076	16	133	0.69
		W	1.691	0.702	85.5	2.440	2.343	39	60	0.57
2015 Nov 30	57356	K	5.398	3.101	−78.9	3.240	3.191	19	166	0.87
		Q	2.681	1.510	−82.2	3.151	3.150	14	222	0.59
		W	1.358	0.745	−85.4	3.084	2.932	32	90	0.53
		D	0.911	0.502	−81.0	2.172	2.150	36	60	0.73
2015 Dec 28	57384	K	5.257	3.138	−86.6	3.702	3.699	41	91	0.73
		Q	2.761	1.513	−82.0	3.635	3.631	24	153	0.58
		W	1.460	0.718	86.9	3.093	3.008	39	76	0.63
		D	0.934	0.497	−86.9	1.809	1.599	34	47	0.58
2016 Jan 13	57400	K	5.171	3.284	80.4	3.227	3.224	28	117	0.58
		Q	2.694	1.529	89.2	2.997	2.983	90	33	0.61
		W	1.386	0.767	80.9	2.519	2.283	25	91	0.51
		D	0.868	0.547	80.5	1.696	1.630	33	49	0.58
2016 Feb 11	57429	K	5.685	3.678	60.2	3.131	3.122	48	65	0.61
		Q	2.835	1.838	58.9	3.433	3.062	53	57	0.62
2016 Mar 1	57448	K	5.343	3.095	−83.1	4.020	3.964	21	192	0.80
		Q	2.686	1.544	−84.6	4.202	4.111	20	207	0.74
		W	1.373	0.750	−87.9	3.328	3.261	34	95	0.68
		D	0.896	0.540	−75.3	2.407	2.363	38	63	0.71
2016 Apr 25	57503	K	5.312	3.308	−78.1	5.461	5.373	61	88	0.72
		Q	2.673	1.627	−78.1	5.243	4.908	28	176	0.65
		W	1.350	0.780	−77.0	3.925	3.832	38	101	0.66
2016 Aug 23	57623	K	5.918	3.101	−66.7	8.440	8.399	50	169	0.69
		W	1.541	0.762	−59.5	4.889	4.916	90	55	0.68
		D	1.019	0.543	−54.5	3.753	3.751	166	23	0.69
2016 Oct 18	57680	K	5.860	2.907	82.7	7.122	6.948	39	180	0.73
		Q	3.180	1.355	82.6	5.657	5.480	29	190	0.83
		W	1.836	0.627	81.4	4.418	4.412	12	383	0.60
		D	1.205	0.426	83.5	3.147	3.149	42	75	0.67
2016 Nov 27	57720	K	5.499	3.472	72.3	6.316	6.370	41	157	0.81
		Q	3.376	1.502	−63.2	5.220	4.653	35	131	0.57
		W	1.703	0.738	−65.2	3.917	3.784	58	65	0.54
2016 Dec 28	57751	K	5.136	3.257	−86.2	8.104	7.729	29	269	0.57
		Q	2.689	1.561	−82.7	6.786	6.375	26	244	0.74
		W	1.311	0.794	84.2	5.909	4.983	43	117	0.67
		D	0.866	0.579	−78.9	3.684	3.689	77	48	0.67

Note. Column designation: 1—date; 2—modified Julian date; 3—observing frequency band: K—22 GHz band; Q—43 GHz band; W—86 GHz band; D—129 GHz band; 4–6—restoring beam: 4—major axis (mas); 5—minor axis (mas); 6—position angle of the major axis (degree); 7—total cleaned KVN flux density (Jy); 8—peak flux density (Jy beam^{-1}); 9—off-source rms in the image (mJy beam^{-1}); 10—dynamic range of the image; 11—quality of the residual noise in the image (i.e., ratio of the image rms noise to its mathematical expectation).

(This table is available in machine-readable form.)

peak to rms) of the image D, and image quality factor ξ_r. The circular Gaussian model-fit parameters, total flux density S_{tot}, peak flux density S_{peak}, size of the core component d, and brightness temperature T_b are given in Table 2.

2.4. OVRO 15 GHz Data

We collected the 15 GHz light curve observed by the Owens Valley Radio Observatory (OVRO) 40 m Telescope. Since late 2007, the OVRO telescope has been operating monitoring observations of about 1500 blazars. The mean cadence of the monitoring is twice a week with a typical error on the flux

density of 4 mJy and systematic uncertainty of 3% (Richards et al. 2011; Max-Moerbeck et al. 2012).[12] The data span we used in this paper is from 2013 January 1 (MJD 56301) to 2016 December 28 (MJD 57750).

2.5. SMA 225 GHz Data

To extend the multifrequency data of the source to higher frequencies, we collected Submillimeter Array (SMA) 1 mm monitoring data. The SMA is an interferometer composed of

Table 2
Modelfit Parameters for the Center of Images

Epoch (1)	MJD (2)	Band (3)	S_{tot} (4)	S_{peak} (5)	d (6)	T_b (7)
2013 Jan 16	56308	K	3.54 ± 0.05	3.40 ± 0.04	0.85 ± 0.01	0.90 ± 0.02
		Q	3.73 ± 0.09	3.60 ± 0.06	0.40 ± 0.01	4.41 ± 0.15
		W	2.68 ± 0.55	2.71 ± 0.39	<0.14	>25.86
		D	2.56 ± 0.57	2.60 ± 0.41	<0.15	>20.14
2013 Mar 28	56379	K	5.58 ± 0.03	5.58 ± 0.02	0.14 ± 0.00	55.09 ± 0.39
		D	6.25 ± 0.71	2.83 ± 0.29	1.29 ± 0.13	0.70 ± 0.14
2013 Apr 11	56393	K	5.05 ± 0.10	4.95 ± 0.07	0.60 ± 0.01	2.63 ± 0.08
		Q	4.42 ± 0.17	4.21 ± 0.12	0.45 ± 0.01	4.13 ± 0.24
		W	4.03 ± 0.78	2.36 ± 0.39	0.74 ± 0.12	1.38 ± 0.46
		D	4.18 ± 2.25	1.30 ± 0.66	0.80 ± 0.41	1.21 ± 1.24
2013 May 7	56419	K	3.96 ± 0.46	3.98 ± 0.33	<0.32	>7.15
		Q	3.34 ± 0.11	3.22 ± 0.08	0.42 ± 0.01	3.53 ± 0.17
		W	2.90 ± 0.13	2.38 ± 0.09	0.45 ± 0.02	2.63 ± 0.19
		D	2.23 ± 0.09	1.83 ± 0.05	0.30 ± 0.01	4.49 ± 0.26
2013 Sep 24	56559	K	4.14 ± 0.08	4.01 ± 0.06	0.75 ± 0.01	1.36 ± 0.04
		Q	2.87 ± 0.18	2.86 ± 0.13	0.16 ± 0.01	21.87 ± 1.95
2013 Oct 15	56580	K	4.03 ± 0.12	3.87 ± 0.08	0.98 ± 0.02	0.77 ± 0.03
		Q	3.57 ± 0.25	2.97 ± 0.16	1.03 ± 0.05	0.63 ± 0.07
		W	2.83 ± 0.15	2.43 ± 0.10	0.41 ± 0.02	3.11 ± 0.25
		D	2.88 ± 0.14	2.45 ± 0.09	0.43 ± 0.02	2.87 ± 0.21
2013 Nov 19	56615	K	4.75 ± 0.06	4.69 ± 0.04	0.49 ± 0.00	3.72 ± 0.07
		Q	3.84 ± 0.06	3.68 ± 0.04	0.43 ± 0.01	3.90 ± 0.09
		W	2.91 ± 0.11	2.58 ± 0.07	0.35 ± 0.01	4.48 ± 0.26
		D	1.94 ± 0.11	1.81 ± 0.07	0.19 ± 0.01	10.06 ± 0.82
2013 Dec 24	56650	K	3.06 ± 0.42	3.08 ± 0.30	<0.37	>4.21
		Q	2.43 ± 0.04	2.41 ± 0.03	0.20 ± 0.00	11.36 ± 0.25
		W	1.96 ± 0.08	1.81 ± 0.05	0.27 ± 0.01	4.90 ± 0.28
		D	1.32 ± 0.30	1.34 ± 0.22	<0.10	>22.99
2014 Jan 27	56684	K	2.75 ± 0.28	2.76 ± 0.20	<0.28	>6.55
		Q	2.32 ± 0.02	2.28 ± 0.01	0.27 ± 0.00	5.81 ± 0.06
2014 Feb 28	56716	K	2.93 ± 0.48	2.96 ± 0.34	<0.46	>2.62
		Q	2.59 ± 0.47	2.61 ± 0.33	<0.25	>7.55
		W	2.09 ± 0.38	2.11 ± 0.27	<0.14	>20.90
		D	1.87 ± 0.09	1.59 ± 0.06	0.24 ± 0.01	6.02 ± 0.45
2014 Mar 22	56738	K	2.77 ± 0.02	2.77 ± 0.02	0.10 ± 0.00	49.30 ± 0.62
		Q	2.67 ± 0.34	2.68 ± 0.24	<0.17	>16.25
		W	2.45 ± 0.52	2.47 ± 0.37	<0.15	>21.05
		D	1.69 ± 0.12	1.64 ± 0.08	0.11 ± 0.01	24.02 ± 2.40
2014 Apr 22	56769	K	4.14 ± 0.45	4.16 ± 0.32	<0.30	>8.73
		Q	4.65 ± 1.49	4.76 ± 1.07	<0.45	>4.30
		W	5.22 ± 0.09	4.86 ± 0.06	0.26 ± 0.00	13.86 ± 0.36
		D	3.98 ± 0.10	3.69 ± 0.07	0.18 ± 0.00	21.78 ± 0.84
2014 Sep 1	56902	K	4.96 ± 0.04	4.74 ± 0.02	0.91 ± 0.00	1.11 ± 0.01
		Q	4.50 ± 0.10	4.24 ± 0.07	0.50 ± 0.01	3.29 ± 0.11
		W	3.78 ± 0.16	3.35 ± 0.10	0.34 ± 0.01	5.98 ± 0.37
		D	3.79 ± 0.13	3.38 ± 0.09	0.33 ± 0.01	6.33 ± 0.32
2014 Oct 29	56960	K	5.62 ± 0.08	5.49 ± 0.05	0.65 ± 0.01	2.46 ± 0.05
		Q	4.86 ± 0.07	4.66 ± 0.05	0.45 ± 0.00	4.55 ± 0.10
		W	3.46 ± 0.22	3.14 ± 0.15	0.29 ± 0.01	7.83 ± 0.73
		D	1.33 ± 0.32	1.35 ± 0.23	<0.14	>12.61
2014 Nov 28	56990	K	5.62 ± 0.99	5.02 ± 0.66	1.20 ± 0.16	0.72 ± 0.19
		Q	4.43 ± 0.18	4.43 ± 0.13	<0.06	>267.51
		W	3.96 ± 0.05	3.34 ± 0.04	0.39 ± 0.00	4.87 ± 0.10
2014 Dec 25	57017	K	5.62 ± 0.04	5.61 ± 0.02	0.16 ± 0.00	39.17 ± 0.35
2015 Feb 23	57076	K	7.07 ± 0.71	7.09 ± 0.50	<0.27	>17.39
		Q	5.76 ± 0.04	5.74 ± 0.03	0.12 ± 0.00	79.23 ± 0.78
		W	4.46 ± 0.12	4.28 ± 0.08	0.20 ± 0.00	19.66 ± 0.75
		D	3.84 ± 1.82	1.07 ± 0.49	1.19 ± 0.54	0.50 ± 0.46
2015 Mar 26	57107	K	5.13 ± 0.06	5.05 ± 0.04	0.50 ± 0.00	3.85 ± 0.06
		Q	4.72 ± 0.05	4.62 ± 0.04	0.30 ± 0.00	9.77 ± 0.16
		W	4.47 ± 0.16	3.94 ± 0.11	0.35 ± 0.01	6.83 ± 0.38
		D	3.30 ± 0.09	3.01 ± 0.06	0.21 ± 0.00	14.26 ± 0.58
2015 Apr 30	57142	K	4.83 ± 0.73	4.88 ± 0.52	<0.41	>5.23

Table 2
(Continued)

Epoch (1)	MJD (2)	Band (3)	$S_{\rm tot}$ (4)	$S_{\rm peak}$ (5)	d (6)	$T_{\rm b}$ (7)
		W	3.38 ± 0.14	3.22 ± 0.09	0.22 ± 0.01	13.31 ± 0.78
		D	2.55 ± 0.04	2.51 ± 0.03	0.08 ± 0.00	68.62 ± 1.61
2015 Sep 24	57289	K	3.30 ± 0.52	3.34 ± 0.37	*<0.42*	*>3.43*
		Q	2.47 ± 0.02	2.45 ± 0.02	0.17 ± 0.00	16.20 ± 0.21
		W	2.01 ± 0.09	1.75 ± 0.06	0.36 ± 0.01	2.90 ± 0.19
2015 Oct 23	57318	K	2.43 ± 0.31	2.45 ± 0.22	*<0.35*	*>3.67*
		Q	2.21 ± 0.07	2.04 ± 0.05	0.56 ± 0.01	1.29 ± 0.06
		W	2.77 ± 0.07	2.34 ± 0.05	0.41 ± 0.01	3.09 ± 0.12
2015 Nov 30	57356	K	3.14 ± 0.50	3.18 ± 0.35	*<0.43*	*>3.11*
		Q	3.14 ± 0.31	3.15 ± 0.22	*<0.13*	*>32.90*
		W	3.11 ± 0.14	2.92 ± 0.10	0.25 ± 0.01	9.51 ± 0.63
		D	2.06 ± 0.90	2.15 ± 0.65	*<0.20*	*>9.79*
2015 Dec 28	57384	K	3.69 ± 0.35	3.70 ± 0.25	*<0.26*	*>10.13*
		Q	3.75 ± 0.30	3.63 ± 0.21	0.34 ± 0.02	5.90 ± 0.67
		W	3.50 ± 0.13	3.00 ± 0.09	0.38 ± 0.01	4.42 ± 0.25
		D	1.90 ± 0.19	1.58 ± 0.12	0.28 ± 0.02	4.33 ± 0.66
2016 Jan 13	57400	K	3.20 ± 0.49	3.22 ± 0.35	*<0.42*	*>3.41*
		Q	3.56 ± 0.28	2.98 ± 0.18	0.85 ± 0.05	0.91 ± 0.11
		W	2.94 ± 0.27	2.28 ± 0.16	0.52 ± 0.04	2.05 ± 0.29
		D	1.70 ± 0.09	1.63 ± 0.06	0.14 ± 0.01	14.98 ± 1.15
2016 Feb 11	57429	K	3.30 ± 0.09	3.12 ± 0.06	1.11 ± 0.02	0.49 ± 0.02
		Q	4.22 ± 0.20	3.20 ± 0.12	1.25 ± 0.05	0.50 ± 0.04
2016 Mar 1	57448	K	3.91 ± 0.57	3.95 ± 0.40	*<0.39*	*>4.67*
		Q	4.39 ± 0.04	4.11 ± 0.02	0.53 ± 0.00	2.91 ± 0.04
		W	3.50 ± 0.08	3.26 ± 0.06	0.27 ± 0.00	9.02 ± 0.32
		D	2.30 ± 0.68	2.35 ± 0.48	*<0.14*	*>23.04*
2016 Apr 25	57503	K	5.28 ± 1.30	5.37 ± 0.92	*<0.68*	*>2.09*
		Q	5.40 ± 0.24	4.89 ± 0.16	0.67 ± 0.02	2.25 ± 0.15
		W	4.03 ± 0.05	3.83 ± 0.03	0.23 ± 0.00	13.53 ± 0.22
2016 Aug 23	57623	K	8.39 ± 0.24	8.39 ± 0.17	*<0.08*	*>237.56*
		W	4.94 ± 0.05	4.92 ± 0.03	0.06 ± 0.00	237.71 ± 3.33
		D	3.56 ± 1.82	3.75 ± 1.32	*<0.25*	*>10.40*
2016 Oct 18	57680	K	6.86 ± 1.26	6.93 ± 0.90	*<0.50*	*>4.98*
		Q	5.98 ± 0.21	5.46 ± 0.14	0.57 ± 0.02	3.36 ± 0.18
		W	4.53 ± 0.04	4.41 ± 0.03	0.14 ± 0.00	39.85 ± 0.56
		D	3.13 ± 0.52	3.15 ± 0.37	*<0.08*	*>93.26*
2016 Nov 27	57720	K	6.27 ± 1.49	6.37 ± 1.06	*<0.69*	*>2.44*
		Q	5.56 ± 0.36	4.55 ± 0.23	0.94 ± 0.05	1.16 ± 0.12
		W	3.88 ± 0.09	3.78 ± 0.07	0.17 ± 0.00	25.44 ± 0.88
2016 Dec 28	57751	K	7.54 ± 1.55	7.62 ± 1.10	*<0.56*	*>4.45*
		Q	6.85 ± 0.24	6.29 ± 0.16	0.60 ± 0.02	3.56 ± 0.18
		W	5.04 ± 0.31	4.84 ± 0.21	0.21 ± 0.01	21.37 ± 1.89
		D	3.66 ± 0.44	3.68 ± 0.31	*<0.06*	*>207.79*

Note. All the modelfit parameters are for the core component at the center of the image. Column designation: 1—date; 2—modified Julian date; 3—observing frequency band: K—22 GHz band; Q—43 GHz band; W—86 GHz band; D—129 GHz band; 4—model flux density of the component (Jy); 5—peak brightness of an individual component measured in the image (Jy beam^{-1}); 6—size (mas), italic numbers indicate upper limits; 7—measured brightness temperature (10^9 K), italic numbers indicate lower limits.

(This table is available in machine-readable form.)

eight telescopes located near the summit of Maunakea, Hawaii. OJ 287 is one of more than 400 sources that are monitored at 1.3 mm and 850 μm wavelengths. Observations of available potential calibrators are from time to time observed for 3–5 minutes, and the measured source signal strength is calibrated by using known standards, typically solar system objects (Titan, Uranus, Neptune, or Callisto). More detailed explanations for the monitoring program of calibrators are described in Gurwell et al. (2007). Data from the program are updated regularly and are available at the SMA website.[13] We

---

[13] http://sma1.sma.hawaii.edu/callist.html

exploited the 1 mm SMA data of OJ 287 from 2013 January 24 (MJD 56317) to 2016 October 13 (MJD 57513).

2.6. VLBA 43 GHz Data

OJ 287 has been conducted with the VLBA observations as part of the VLBA Boston University monthly monitoring program at 43 GHz (Jorstad et al. 2005). We used the data only to analyze the magnetic field strengths in this work from 2014 January 20 (MJD 56677) to 2016 March 19 (MJD 57466). In order to estimate the size and flux density of emission features
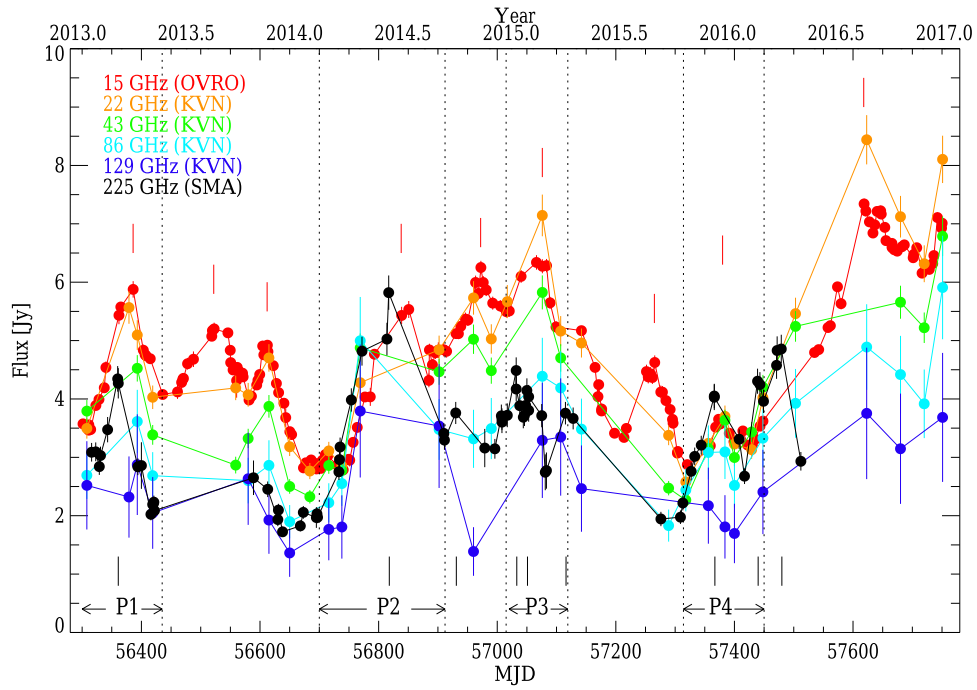
Figure 2. Light curves of OJ 287 from 15 to 225 GHz observed from 2013 January until 2017 December. Red, yellow, green, sky blue, blue, and black symbols correspond to flux density at 15, 22, 43, 85, 129, and 225 GHz, respectively. The red and black bars indicate local peaks at 15 and 225 GHz, respectively. Local peaks are labeled as P1, P2, P3, and P4, respectively, and are also marked by dotted lines and horizontal arrows.

within the map, we fitted circular Gaussians using the MODELFIT task in Difmap.

3. Results

3.1. VLBI Morphology

Typically a blazar jet exhibits a core-jet structure. The core is usually defined as the bright compact region that is observed at the most upstream point of the jet (Jorstad et al. 2017). Jet emission is observed to move out from the core. At high resolution OJ 287 is known to have a core and also a downstream quasi-stationary feature (Agudo et al. 2012; Hodgson et al. 2016). The source at all KVN observing frequencies is unresolved appearing point-like, with no jet emission and also the quasi-stationary feature unresolved (see, Figure 1). We therefore refer to the bright unresolved region in the KVN maps as the core.

3.2. Multifrequency Light Curves

We present the results and analysis of the flux density variability at multiple frequencies. Figure 2 shows multi-frequency light curves of OJ 287 at 15 GHz (OVRO), 22–129 GHz (KVN), and 225 GHz (SMA) observed between 2013 January 16 (MJD 56308) to 2016 December 28 (MJD 57750). The light curves show several flux enhancements over four years. We found nine local peaks at 15 GHz on MJD 56386, 56522, 56612, 56838, 56972, 57076, 57265, 57380, and 57618 and nine local peaks at 225 GHz on MJD 56361, 56818, 56931, 57033, 57051, 57116, 57367, 57440, and 57480. These local peaks are indicated by red vertical bars for 15 GHz and black for 225 GHz. We selected four parts (P1, P2, P3, and P4), which include local peaks in the KVN data also. These parts are marked within the dotted line sections as shown in Figure 2, in order to analyze the properties of the variability in flux density.

3.2.1. The 15 GHz Light Curves

The light curve at 15 GHz with a mean cadence of 8 days shows 9 local peaks over ~4 yr in Figure 2. Over the period between MJD 56301 and 56673, three local peaks appeared and then the flux density was observed to be at a minimum of roughly 3 Jy, which lasted ~70 days. The first local peak was designated as P1. From MJD 56740 until 57320, four local peaks occurred and then the flux density was again observed to be at a minimum of roughly 3 Jy. The first peak and the third peak of the five peaks were named as P2 and P3, respectively. Between MJD 57320 and 57450, one small local peak (named P4) appeared on MJD 57380 and then the flux density significantly increased and local peak flux density of 7.3 Jy was observed on MJD 57618. In summary, the 15 GHz light curve of OJ 287 shows nine flux enhancements, ranging from roughly 3 to 7.3 Jy with a mean flux density of 4.7 Jy over four years.

3.2.2. The 225 GHz Light Curves

The SMA 225 GHz light curve has periods of high cadence but also periods with sparse observations. Several of the flux enhancements observed at 15 GHz were not traced but the trend of the light curve follows the 15 GHz light curve quite well. Over the period between MJD 56301 and 56450 (P1), the first local peak appeared with flux density of 4.3 Jy. The light curve of 225 GHz shows a major flux enhancement between MJD 56638 and MJD 56911 (P2) and subsequent flux enhancements appeared between MJD 57015 and 57119 (P3), and MJD 57314 and 57450 (P4). The minimum and maximum flux densities at 225 GHz are 1.7 Jy and 5.8 Jy, respectively.

3.2.3. The 22–129 GHz Light Curves

The light curves at 22–129 GHz were obtained simulta-neously at an average monthly interval using the KVN. The

Table 3
Fractional Variability

Frequency (GHz)	F_{var}
15	0.27 ± 0.003
22	0.33 ± 0.013
43	0.30 ± 0.012
86	0.25 ± 0.089
129	0.04 ± 0.33
225	0.28 ± 0.021

number of available flux density measurements are 31 at 22 GHz, 27 at 43 GHz, 25 at 86 GHz, and 19 at 129 GHz.

Despite the relatively low cadence of the KVN observations, the trend of the KVN light curves is similar to the 15 GHz and the 225 GHz light curves (i.e., following increasing and decreasing trends, and showing the corresponding local minima of the flux density). The minimum and maximum flux densities are 2.6 Jy and 8.4 Jy at 22 GHz, 2.3 Jy and 6.8 Jy at 43 GHz, 1.8 Jy and 5.9 Jy at 86 GHz, and 1.4 Jy and 3.8 Jy at 129 GHz, respectively. The mean flux densities are 4.6 Jy, 4.0 Jy, 3.4 Jy, and 2.5 Jy at 22, 43, 86, and 129 GHz, respectively.

3.3. Fractional Variability Amplitude

There are several ways of measuring the amplitude of the flux density variability of blazar sources, such as the variability index $(V = (S_{\max} - S_{\min})/(S_{\max} + S_{\min})$; $S_{\max}$ and $S_{\min}$ are maximum flux density and minimum flux density, respectively; Aller 1999), the modulation index ($m = 100 \cdot \sigma_s/\langle S \rangle$; σ_s and $\langle S \rangle$ are rms of the flux density and mean flux density, respectively; Kraus et al. 2003), and the fractional variability amplitude (Edelson et al. 2002). We adopted the fractional variability amplitude method, which can additionally correct noise effects from the measurement errors (Chidiac et al. 2016). The fractional variability amplitude, F_{var}, is defined as

$$F_{\mathrm{var}} = \sqrt{\frac{V - \overline{\sigma_{\mathrm{err}}^2}}{\bar{S}^2}}, \qquad (1)$$

where V, $\overline{\sigma_{\mathrm{err}}^2}$, and $\bar{S}$ are the variance of the flux density, mean squared error, and mean flux density, respectively. The uncertainty of the fractional variability is given by

$$\mathrm{err}(F_{\mathrm{var}}) = \sqrt{\left(\sqrt{\frac{1}{2N}}\frac{\overline{\sigma_{\mathrm{err}}^2}}{\bar{S}^2 F_{\mathrm{var}}}\right)^2 + \left(\sqrt{\frac{\overline{\sigma_{\mathrm{err}}^2}}{N}}\frac{1}{\bar{S}}\right)^2}. \qquad (2)$$

In Table 3 we listed the estimated values of the fractional variability at 15–225 GHz. For the 129 GHz data, we could not calculate the fractional variability amplitude due to large measurement errors, which is larger than the variance of the flux density. Therefore, we exclude the 129 GHz data in the analysis. The range of F_{var} was 0.25–0.33, which was relatively constant within the observing frequencies from 15 to 225 GHz (see Figure 3). This suggested that there were not significant variations in F_{var} in the frequency domain.

3.4. Variability Time Scales at 15 and 225 GHz

In order to estimate the timescales of the individual flux enhancements, the light curves were linearly interpolated to 1 day intervals and then we employed the structure function (SF) to estimate the variability timescale as defined by
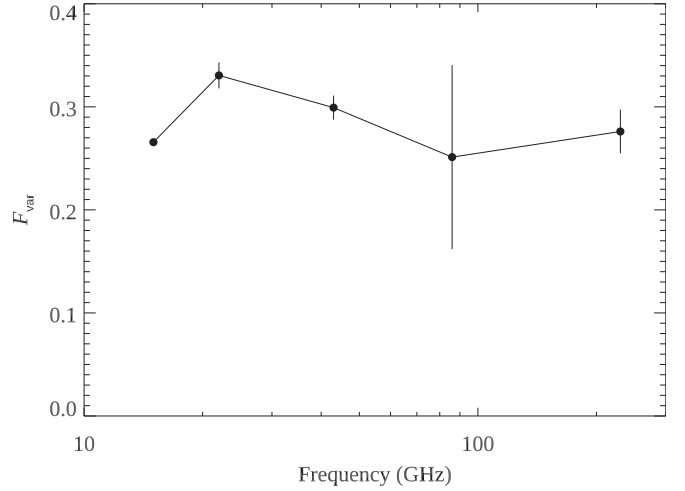
Figure 3. Fractional variability as a function of frequency of OJ 287.

Simonetti et al. (1985) and Heeschen et al. (1987):

$$\mathrm{SF}(\tau) = \frac{1}{N}\sum_{i=1}^{N}[f(t_i) - f(t_i + \tau)]^2, \qquad (3)$$

where $f(t_i)$, τ, and N are the flux density at time t_i, the time lag, and the number of data points, respectively. The SF curves for P1–P4 at 15 GHz and 230 GHz are presented in Figure 4. For the other frequencies (22–129 GHz), the data are sparse and therefore we cannot find reliable timescales for P1 to P4, individually. The SF curves show a steeply rising trend to the first peak corresponding to characteristic timescale. For P3 at 225 GHz, the SF curve shows a double peak curve, which indicates that there might be double peaks in the light curves. We used the second peak as it is considerably more significant.

We obtained timescales τ_{var} of 62 ± 8 days at 15 GHz and 51 ± 8 days at 225 GHz for P1, 128 ± 12 days at 15 GHz and 119 ± 21 days at 225 GHz for P2, 51 ± 10 days at 15 GHz and 51 ± 5 days at 225 GHz for P3, 49 ± 8 days at 15 GHz and 48 ± 12 days at 225 GHz for P4 of the timescales τ_{var} from the estimation of the SF as summarized in Table 4. Here the errors of the timescales indicate the median interval of light curves. The corresponding SF values at the peak are 2.2, 4.9, 0.38, and 0.16 at 15 GHz for P1–P4, respectively, and 1.4, 4.3, 0.49, and 0.73 at 225 GHz for P1–P4, respectively, as marked with red dotted lines in Figure 4. The estimated timescales of the three flux enhancements P1, P3, and P4 are similar with a timescale of $\sim$50 days at two frequencies, but the timescale of P2 is twice as long at the high frequency. Since the SF value is proportional to the square of the amplitude of the flux enhancement, the strength of the flux enhancements for P1 and P2 is relatively larger in comparison with those of P3 and P4.

4. Analysis

4.1. Spectral Index

The iMOGABA program facilitates spectral index studies, since the observations at the various frequencies within the program are exactly simultaneous. Figure 5 shows the spectral index as a function of time for pairs of the KVN frequencies. The spectral indices are variable as a function of time in the range of -0.5 ± 0.2 to 0.2 ± 0.2 between 22 and 43 GHz with
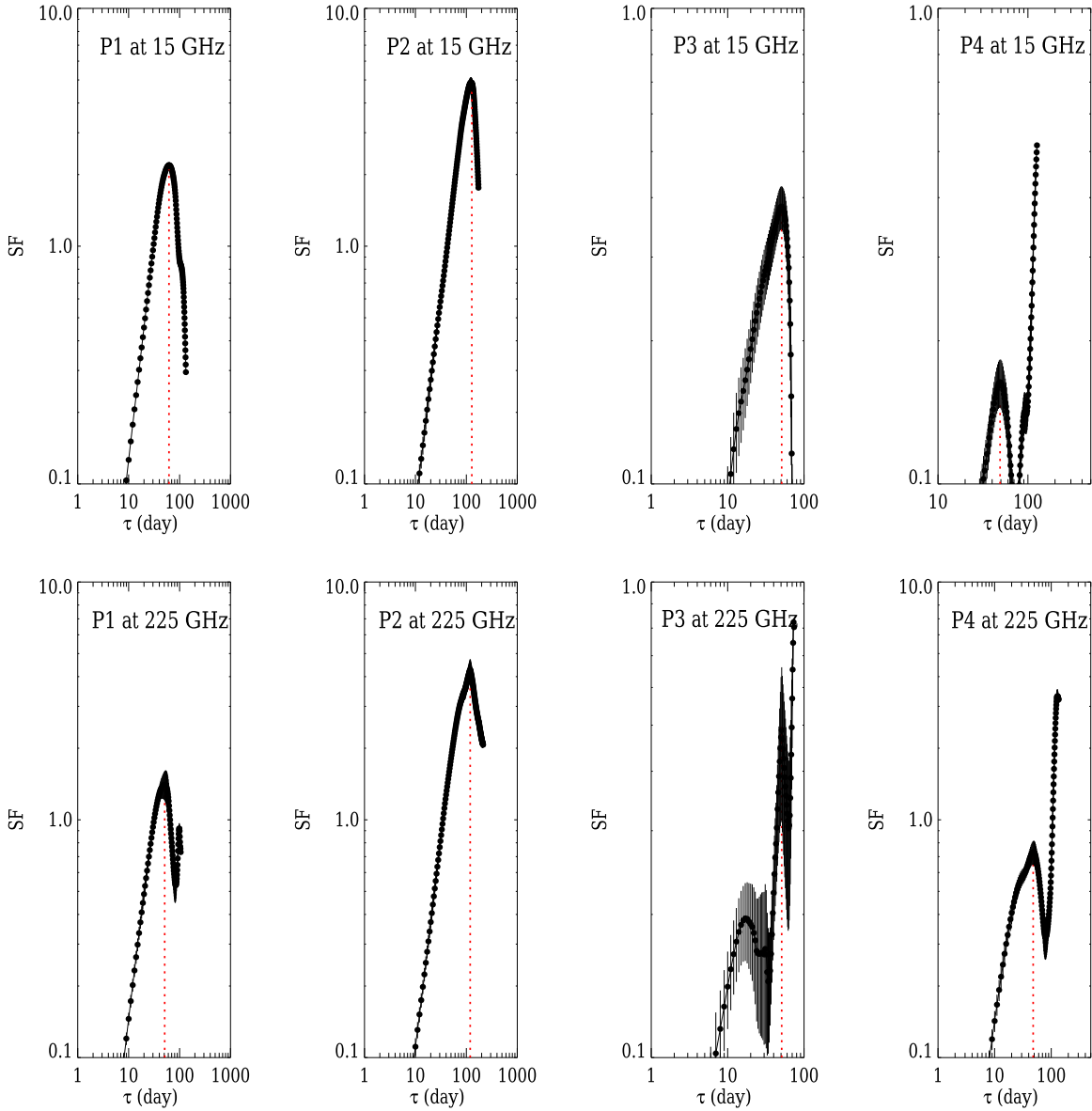
Figure 4. Structure function of OJ 287 light curves at multiple radio frequencies. Top is P1–P4 at 15 GHz, bottom is P1–P4 at 225 GHz. Red dotted lines indicate timescales.

mean spectral index, $\langle\alpha\rangle_{22-43}$, of -0.2, -0.6 ± 0.3 to 0.1 ± 0.3 between 43 and 86 GHz with $\langle\alpha\rangle_{43-86}$ of -0.3, -2.2 ± 0.8 to 0.04 ± 0.8 between 86 and 129 GHz with $\langle\alpha\rangle_{86-129}$ of -0.8. The spectral indices are mostly negative (i.e., optically thin) with a mean index as listed in Table 5. The spectral index analysis implies that the source has an optically thin spectrum at millimeter wavelengths.

4.2. Physical Parameters from the Variability Time Scales

4.2.1. Apparent Brightness Temperature

Assuming that the component causing the flux variation has a spherical brightness distribution, its apparent brightness temperature can be estimated following Rani et al. (2013) as

$$T_{\rm B,var} = 3.47 \times 10^5 \times \Delta S \left(\frac{\lambda D_L}{\tau_{\rm var}(1+z)^2} \right)^2, \qquad (4)$$

where ΔS is the variation of the flux density in Jy over a variability timescale, $\tau_{\rm var}$ in years, which was obtained from the structure function analysis in Section 3.4, λ is the observing wavelength in centimeters, D_L is the luminosity distance in megaparsecs, and z is the redshift. Here we adopt $D_L = 1630$ Mpc. The values of $\tau_{\rm var}$ and ΔS are listed in Table 4. We obtain apparent brightness temperatures $T_{\rm B,var}$ of $(2.4–9.0) \times 10^{14}$ K at 15 GHz and $(1.6–5.5) \times 10^{12}$ K at 225 GHz for P1–P4 as listed in Table 4. We found that the $T_{\rm B,var,15}$ is higher than $T_{\rm B,var,225}$ in all flux enhancements.

4.2.2. Doppler Factor

We obtained brightness temperature measurements at 15 and 225 GHz in Section 4.2.1. If we assume that there is a maximum intrinsic brightness temperature, $T_{\rm B,int}$, that can be achieved by the source we can estimate the Doppler factor of the source with the following expression (Rani et al. 2013;

Table 4
Variability Time Sale, Apparent Brightness Temperature, Doppler Factor, Size, Time Delay, and DCF

			P1				
ν (GHz)	$\tau_{\rm var}$ (days)	ΔS (Jy)	$T_{\rm B,var}$ (K)	$\delta_{\rm var}$	$\theta_{\rm var}$ (mas)	τ (day)	DCF
15	62 ± 8	2.4 ± 0.8	9.0×10^{14}	7.8	0.067	-23 ± 12.7	0.8
225	51 ± 8	2.3 ± 0.7	5.4×10^{12}	2.0	0.014		
			P2				
15	128 ± 12	2.7 ± 0.9	2.4×10^{14}	5.5	0.098	-30.6 ± 5.1	0.7
225	119 ± 21	3.8 ± 1.2	1.6×10^{12}	1.5	0.025		
			P3				
15	51 ± 10	1.1 ± 0.4	6.1×10^{14}	7.1	0.050	-14.8 ± 4.7	0.7
225	51 ± 5	1.7 ± 0.5	4.0×10^{12}	1.9	0.013		
			P4				
15	49 ± 8	0.8 ± 0.2	4.6×10^{14}	6.6	0.045	-7.0 ± 9.4	0.8
225	48 ± 12	2.1 ± 0.7	5.5×10^{12}	2.0	0.014		
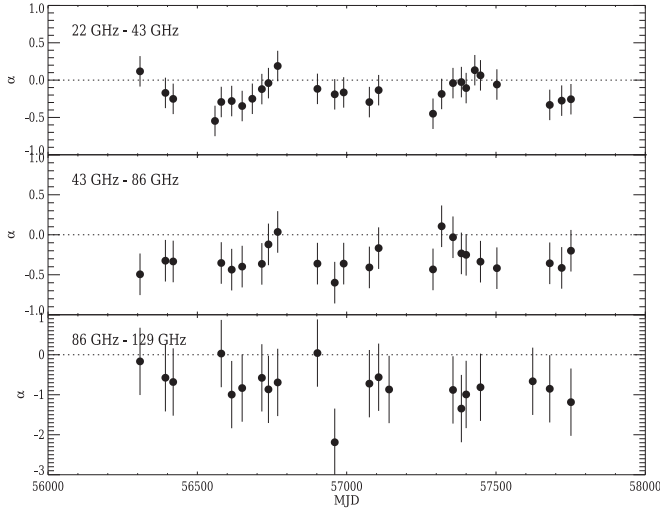
Figure 5. Spectral indices of OJ 287. Top, middle, and bottom panels correspond to spectral indices estimated between 22 and 43 GHz, 43 and 86 GHz, and 86 and 129 GHz, respectively.

Table 5
Mean Spectral Index

Frequency Pair	Mean Spectral Index
22–43 GHz	$-(0.15 \pm 0.20)$
43–86 GHz	$-(0.32 \pm 0.26)$
86–129 GHz	$-(0.79 \pm 0.84)$

Lee et al. 2017a):

$$\delta_{\rm var} = (1 + z)\left(\frac{T_{\rm B}^{\rm app}}{T_{\rm B,int}}\right)^{1/(3+\alpha)}, \qquad (5)$$

where α is the spectral index of optically thin regions. We adopted $\alpha = -0.8$ from the mean spectral index between 86 and 129 GHz in our observations (see Section 4.1). The Doppler factors estimated depend on the value chosen for $T_{\rm B,int}$. We have conservatively assumed a value of 10^{12} K, which is the inverse Compton limit (Kellermann & Pauliny-Toth 1969). If the intrinsic brightness temperature limit is lower than 10^{12} K, this would increase the estimated values of the Doppler factors. The estimated Doppler factors are in the ranges of 5.5–7.8 at 15 GHz and 1.5–2.0 at 225 GHz for P1–P4 as listed in Table 4. The Doppler factors at 15 GHz are higher than at 225 GHz by a factor of at least ~3. This implies that the emitting regions at two frequencies may be different.

4.2.3. Size of the Emitting Region

Assuming that the variability of the flux density is intrinsic to the source, we can use causality arguments to estimate the size of the emitting region. We can therefore compute the size of the emitting region, $\theta_{\rm var}$ Rani et al. (2013):

$$\theta_{\rm var} = 0.173\frac{\tau_{\rm var}}{D_L}\delta_{\rm var}(1 + z), \qquad (6)$$

where $\tau_{\rm var}$ is the timescale in days, D_L is luminosity distance in megaparsecs and $\delta_{\rm var}$ is the Doppler factor. The calculated sizes of emitting region are in the ranges of 0.058–0.128 mas at 15 GHz and 0.017–0.032 mas at 225 GHz for P1–P4 as tabulated in Table 4. The estimated sizes of emitting regions change according to the periods by a factor of 2 at 15 GHz and 225 GHz. The mean sizes from the VLBA at 43 GHz is 0.032 ± 0.02 mas (Jorstad et al. 2017) and from the GMVA at 86 GHz is 0.035 ± 0.02 mas (Hodgson et al. 2017). The estimated $\theta_{\rm var}$ compares well with the sizes obtained from these VLBI observations.

4.3. Discrete Cross-correlation

Multifrequency light curves enable us to study correlations with a time lag between different frequencies. In order to compute the time lag between the flux density variability at 15 and 225 GHz, we used the discrete cross-correlation function (DCF), which is defined by Edelson & Krolik (1988). A detailed description of the DCF can be found in Edelson & Krolik (1988) and Lee et al. (2017a). To calculate the DCF, we first compute unbinned discrete correlations (UDCF) for two
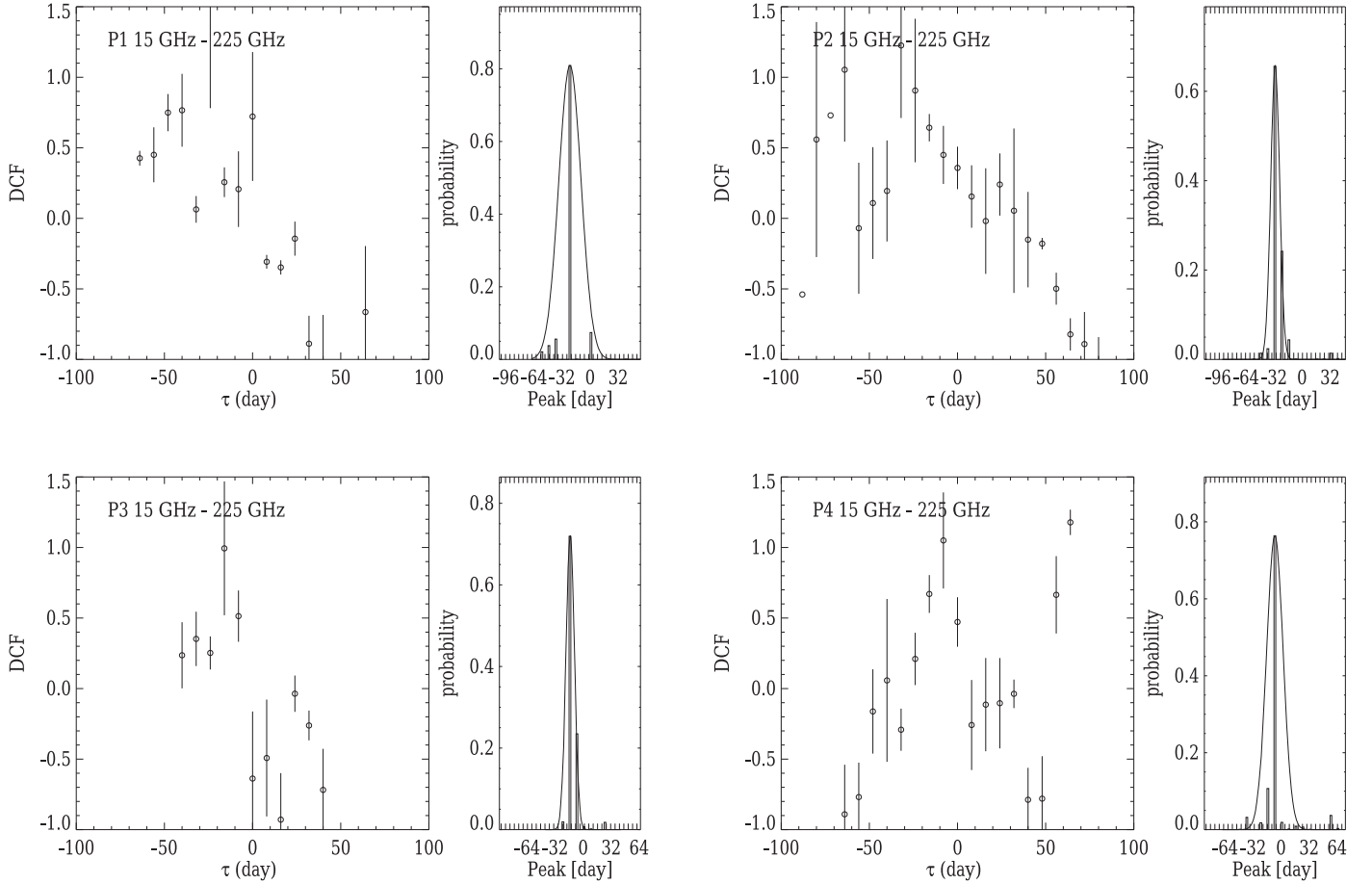
Figure 6. Cross-correlation function and corresponding cross-correlation peak distribution of the light curves at 15 and 225 GHz in OJ 287 for P1–P4.

data sets as follows.

$$\text{UDCF}_{ij} = \frac{(a_i - \bar{a})(b_j - \bar{b})}{\sqrt{\sigma_a^2 - \sigma_b^2}}, \quad (7)$$

where a_i and b_j are the measurements of data sets a and b for each light curve, $\bar{a}$ and $\bar{b}$ are the mean of the data sets, and σ_a and σ_b are their corresponding standard deviations of the time series. The UDCF is binned with an interval $\Delta\tau$ for estimating the DCF

$$\text{DCF}(\tau) = \frac{1}{M} \sum \text{UDCF}_{ij}(\tau), \quad (8)$$

for each time lag, where M is the number of data points in the bin. We estimated the standard error for each bin with the following equation:

$$\sigma_{\text{DCF}}(\tau) = \frac{1}{M-1} \sqrt{\sum [\text{UDCF}_{ij}(\tau) - \text{DCF}(\tau)]^2}. \quad (9)$$

To calculate the DCF, the bin size has to be determined. We chose a minimum interval of 8 days in the light curve at 15 GHz as the bin size. The correlated peak at a certain time in the DCF curves corresponds to the time delay between two light curves. We performed a Monte Carlo simulation to estimate the uncertainty of the time lag obtained from the DCF. We followed the random subset selection method as presented by Peterson et al. (1998) to estimate this uncertainty.

From this method, randomly sampled light curves were generated $N = 1000$ times to calculate the correlated peaks. Therefore, we obtained 1000 time delays and their distribution, that is, cross-correlation peak distribution (CCPD) as shown in the right panel of Figure 6. Then we fitted the Gaussian function into the CCPD to measure the time delay. We obtained the time delay of $-(23.0 \pm 12.7)$ days for the period of P1 in the light curves, $-(30.6 \pm 5.1)$ days for P2, $-(14.7 \pm 4.7)$ days for P3, and $-(7.0 \pm 9.4)$ days for P4. If the CCPD can be assumed to be a normal distribution, a confidence interval of 95%, $\tau_{95\%}$, can be calculated from $\tau - 1.96\frac{\sigma}{\sqrt{N}} < \tau_{95\%} < \tau + 1.96\frac{\sigma}{\sqrt{N}}$. Here τ is time delay, N is number of simulations, and σ is the standard deviation of the CCPD. We found $-23.08 < \tau_{95\%} < -22.92$ for P1, $-30.68 < \tau_{95\%} < -30.52$ for P2, $-14.75 < \tau_{95\%} < -14.65$ for P3, and $-7.12 < \tau_{95\%} < -6.88$ for P4, respectively. The minus sign means that the light curves at 225 GHz lead the one at 15 GHz as shown in the left panel of Figure. 6. All the peaks of flux enhancements at 225 GHz led those at 15 GHz with a time lag of 7–30 days. The obtained time delay τ and the DCF values are listed in Table 4.

4.4. Radio Spectral Energy Distribution

The simultaneous multifrequency observations at four frequencies (22, 43, 86, and 129 GHz) enable us to study the millimeter-wavelength spectra of OJ 287 without uncertainty in the time domain.

The millimeter-wavelength spectrum has been obtained for those epochs when the source CLEAN flux density measurements

are available at two to four frequency bands out of the 22, 43, 86, and 129 GHz bands. The spectrum with two or three measurements were fitted with a simple power-law function and that with four frequency measurements was fitted with a curved power-law function (Lee et al. 2016b, 2017a; Algaba et al. 2018b) as

$$S = c_1 \left(\frac{\nu}{\nu_c} \right)^{a + c_2 \ln(\nu/\nu_c)}, \qquad (10)$$

where S is the CLEAN flux density in Jy, ν is the observing frequency in GHz, ν_c is the turnover frequency, a is the spectral index at ν_c, and c_1 is a constant in Jy. Here a can be considered to be the spectral index of optically thin emission. In 11 epochs, there were fewer than four spectral data points. For these epochs, the spectrum was fitted with a power-law function. For the further 19 epochs, a curved power law was used as it produced a lower reduced χ^2 value. For eight epochs out of the curved power-law fit cases, we obtained turnover frequencies and peak flux densities within the observing frequency range of the KVN (see panels (1) and (2) of Figure 8). The radio spectra of 30 epochs are plotted in Figure 7 and the best-fit results are listed in Table 6. In Figure 7, the spectral index α is obtained from the power-law fits and the turnover frequency ν_c and flux density S_m at the turnover frequency are obtained from the curved power-law fits. All of the spectral indices α are steep with a minus sign in the range from -1.3 to -0.04 and the turnover frequency ν_c is in the range of 27–50 GHz and the peak flux density S_m is in the range of 2.9–5.8 Jy, as summarized in Table 6.

4.5. Synchrotron Self-absorption Magnetic Field Strength

The turnover frequency and peak flux density determined by the spectral model fitting (see Section 4.4) allows us to constrain the magnetic field in the emission region that dominates the flux density at the turnover frequency, assuming that the emission region is a compact and hence a homogeneous synchrotron self-absorption (SSA) region. Following Marscher (1983) and Lee et al. (2017a), we can express B_{SSA} as

$$B_{SSA} = 10^{-5} b(\alpha) S_m^{-2} \theta^4 \nu_c^5 \left(\frac{\delta}{1+z} \right)^{-1} (G), \qquad (11)$$

where $b(\alpha)$ is a parameter that depends on the optically thin spectral index ranging from 1.8 to 3.8 (see Table 1 in Marscher 1983), and θ is 1.8 times the angular size (mas) of the emission region (Marscher 1977; Hodgson et al. 2016). The observed sizes of SSA components are expected to vary as a function of frequency. This relationship under the model suggested by Blandford & Königl (1979) is expected to follow the relationship $\theta \propto \nu^{-\epsilon}$. ϵ is a parameter related to the geometry of the jet. If $\epsilon = 1$, this would mean a fully conical jet and if $0 < \epsilon < 1$, this means the jet is parabolic. Algaba et al. (2017) found a value of $\epsilon = 0.4 \pm 0.1$ for OJ 287. We have adopted that value here. We linearly interpolated the VLBA sizes in time in order to estimate the size at the time of the measurements of the turnover frequency. We therefore used the following expression to estimate the size at the turnover frequency: $\theta_{pred.}/\theta_{43} = (\nu_c/43)^{0.4 \pm 0.1}$. The estimated sizes are listed in Table 6.

The range of θ at the turnover frequency is 0.014–0.065 mas. We note that Equation (11) is revised from the equation in Marscher (1983) with the $(\delta/1 + z)^{-1}$ factor instead of $(\delta/1 + z)$ since the core of the source in the VLBI image map is thought to be quasi-stationary and therefore not moving. The synchrotron self-absorption magnetic field strength was computed by performing $N = 1000$ Monte Carlo simulations via Equation (11), as described in detail in the following. All variables are simulated using a random sample of a normal distribution. The simulated variables and errors indicate the mean values and standard deviation of normal distribution, respectively. The input parameters are θ, δ, ν_c, and S_m and their respective errors. Here, we used the values for θ showing in Table 6 and $\delta = 7.9$ which are obtained from the VLBI observations by Hodgson et al. (2017). The value $b(\alpha)$ depends on the spectral index and its value can be found in Marscher (1983). The appropriate values have been listed in Table 6. We used the turnover frequencies and flux density at the turnover frequency determined in Section 4.4. The measured flux density at the turnover frequency $S_m = 2.9$–5.8 Jy, and the turnover frequency $\nu_c = 27.3$–50.0 GHz, we obtained the magnetic field B_{SSA} ranging from 0.0004 to 0.255 mG, as listed in Table 6 and plotted panel (3) in Figure 8.

Due to the limited resolution of the KVN observations, special care must be taken to ensure that measured parameters are coming from either the core or the downstream quasi-stationary feature (see Section 3.1). To check this, we plotted the flux density of the core and stationary feature in Figure 9 obtained from the VLBA-BU-BLAZAR monthly monitoring program at 43 GHz. Only in epochs 12, 24, and 26 is the emission dominated by the core. The downstream quasi-stationary feature does not dominate the total flux density in any epochs. In these three epochs, the SSA magnetic field strength is measured to be roughly consistent at about 0.255 mG. This is approximately an order of magnitude lower than the magnetic field strength assuming equipartition. In particular, in epoch 12, the turnover frequency was measured to be 50 GHz, which is close to the observing frequency of the BU program and also dominated by the core emission.

4.6. Equipartition Magnetic Field Strength

The magnetic field of the emission regions in the relativistic jet can also be investigated under the assumption that the energy densities of particles and magnetic fields are equal, following Kataoka & Stawarz (2005) as

$$\begin{aligned} B_{eq} &= 0.25 \eta^{2/7} (1+z)^{11/7} D_L^{-2/7} \nu_c^{1/7} \\ &\quad \times S_m^{2/7} \theta^{-6/7} \delta^{-5/7} \quad mG, \end{aligned} \qquad (12)$$

where η is the ratio of energy density carried by protons and electrons to the energy density of the electrons; i.e., the $\eta = 1$ for the leptonic jet (i.e., electron–positron) and $\eta = 1836$ for the hadronic jet (i.e., electron–proton) (Kataoka & Stawarz 2005). The parameters D_L, ν_c, S_m, θ_c, and δ are a luminosity distance in megaparsecs, turnover frequency in GHz, flux density at the turnover frequency in Jy, 1.8 times core size in mas, and Doppler factor, respectively. For $\eta = 1$, the magnetic field would be ~3.8 times weaker and for $\eta = 1836$, it would be ~2.3 times stronger. Here, we use $\eta = 100$. The values
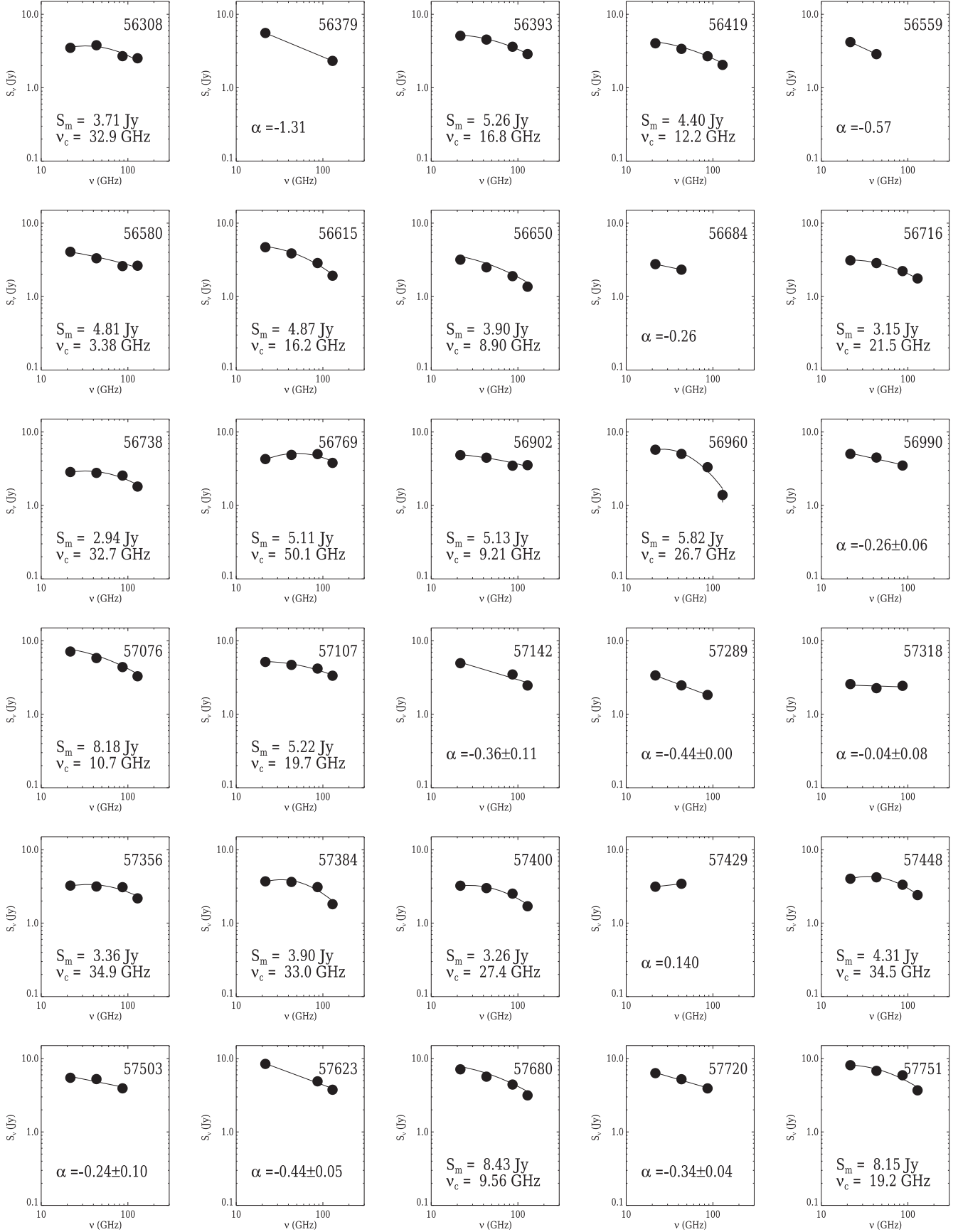
Figure 7. Spectral energy distribution of OJ 287 from 15 to 225 GHz observed over 2013 January to 2017 December. The 16th epoch (MJD 57017) is excluded since there was only one detection at 22 GHz.

Table 6
Flux Density at the Turnover Frequency S_m, Turnover Frequency ν_c, Angular Size, Synchrotron Self-absorption Magnetic Field Strength, and Equipartition Magnetic Field Strength

MJD (day)	Epoch	Date	S_m (Jy)	ν_c (GHz)	$b(\alpha)$	θ (mas)	B_{SSA} (mG)	B_{eq} (mG)
56308	1	2013 Jan 16	3.7 ± 0.1	32.7 ± 3.3	3.1	0.032	0.025 ± 0.025	1.82 ± 0.28
56738	11	2014 Mar 22	2.9 ± 0.1	32.5 ± 3.7	1.8	0.022	0.006 ± 0.007	2.41 ± 0.37
56769	12	2014 Apr 23	5.1 ± 0.1	50.0 ± 2.0	3.5	0.036	0.161 ± 0.146	1.93 ± 0.30
56960	14	2014 Oct 30	5.8 ± 0.1	26.6 ± 2.0	3.8	0.014	0.0004 ± 0.0006	4.03 ± 0.62
57356	22	2015 Nov 30	3.4 ± 0.1	34.7 ± 3.7	1.7	0.063	0.226 ± 0.144	1.02 ± 0.16
57384	23	2015 Dec 28	3.9 ± 0.1	33.0 ± 2.3	3.2	0.061	0.230 ± 0.136	1.07 ± 0.17
57400	24	2016 Jan 13	3.3 ± 0.1	27.3 ± 3.7	3.2	0.065	0.157 ± 0.104	0.95 ± 0.15
57448	26	2016 Mar 1	4.3 ± 0.1	34.4 ± 2.3	2.9	0.065	0.255 ± 0.146	1.06 ± 0.16

Note. Only epochs 12, 24, and 26 are considered reliable for the magnetic field strength. See Section 4.5 for more details.
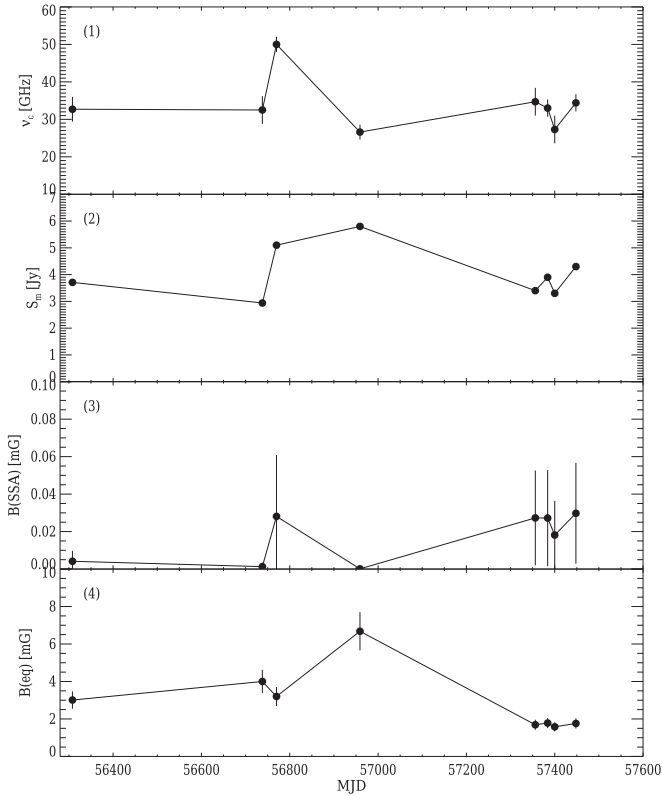
Figure 8. (1) Turnover frequency ν_c, (2) peak flux density S_m, (3) magnetic field strength derived from synchrotron self-absorption, and (4) equipartition magnetic field strength (4) of OJ 287.

Figure 9. Light curves of OJ 28. Black symbols indicate the core and red symbols indicate the stationary component nearest to the core.

of B_{eq} are in the range of 0.95 ± 0.15–4.03 ± 0.62 mG as listed in Table 6 and in panel (4) of Figure 8.

5. Discussion

5.1. Multifrequency Variability Characteristics

The calculated fractional variability amplitude in Section 3.3 shows no trend with frequency, with the exception of the 129 GHz measurement, which may be due to large uncertainties. The lack of a trend could be due to limited time sampling at higher frequencies. To test this possibility, we equalized the number of data points to that at 230 GHz. We then recalculated the fractional variability amplitude and found that there is no

difference in the trend. This constant trend is in contrast to the results of Algaba et al. (2018a) in 1633+382 and the results of Chidiac et al. (2016) in 3C 273. In both of these examples, increasing variability amplitudes were found as a function of increasing frequency which was interpreted as being due to opacity effects. For individual flux enhancements (P1–P4), we performed the F_{var} test on each enhancement. We found that the results of the F_{var} test on individual flux enhancements are similar to that for whole light curves. We confirmed that the results of the F_{var} test on the radio/millimeter light curves of OJ 287 are inconsistent with those for 1633+382 (Algaba et al. 2018a) and 3C 273 (Chidiac et al. 2016).

This inconsistency may be due to the quasi-stationary component of OJ 287. As shown in Figure 9, the trends of variability of the core and the quasi-stationary component are different from each other, resulting in the mixture variability of the integrated light curves obtained with single dish observations or low resolution VLBI observations at 15–225 GHz. For example, the core and the quasi-stationary component vary in flux density differently—the core and the quasi-stationary component get brighter for P2 (MJD 56638−56910), whereas for P4 (MJD 57314−57450) the core gets brighter and the quasi-stationary component gets fainter. The mixture variability of multiple components may not clearly show the frequency dependence of the fractional variability.

5.2. Time Delay between 15 and 225 GHz

The source showed significant correlations in the flux density variability between the 15 and 225 GHz light curves. The variability at the high frequency led that at 15 GHz, which can be interpreted by the opacity effect due to the synchrotron self-absorption of the spectrum. The source is optically thick at 15 GHz and optically thin at 225 GHz. Therefore, the opacity effect plays a role between these frequencies. The obtained time delays between 15 and 225 GHz light curves using the DCF analysis in Section 4.3 are different for individual periods, i.e., 7–30 days for Part 1 to Part 4 (over ~4 yr), the variation of the time delay, which was also reported for 3C 345 (a range of time delay of 0.4–1.8 yr between 5 and 37 GHz over 18 yr) by Kudryavtseva et al. (2011).

The time delay Δt can be described as $\Delta t = d \sin \theta / c \cdot \beta_{\mathrm{app}}$, where d is the distance between emitting regions in the jet, θ is the viewing angle of the jet to the line of sight, c is the speed of light, and β_{app} is the apparent speed of the jet. Jorstad et al. (2017) reported the change of β_{app} in a range of 3.33–8.60 and that of θ in a range of $1°3–8°9$ over ~5 yr.

These variations of those parameters may change the time delay by a factor of <8.8, assuming the distance between emitting regions is constant. If we assume that β_{app} and θ are constant at $8°6$ and $1°3$, respectively, the distance between 15 and 225 GHz emitting regions can be estimated in a range of 2.2–9.7 pc. Furthermore, if we assume the jet is conical at a parsec scale, we can derive the distance of the 225 GHz emitting region to the jet apex using the size of the emitting region. Therefore, the distance from the jet apex to 15 GHz radio emitting regions is in the range of 3.2–12.9 pc. However, in Pushkarev et al. (2012), the authors reported that the distance from the jet apex to the 15 GHz core region was <4.13 pc by using core-shift measurements assuming β_{app} of ~15.2 and Hodgson et al. (2016) reported the distance from the jet apex to the millimeter core is <4–6 pc using a magnetic field relation of $B \propto r^{-1}$. In some cases, the distance we estimated is larger than the value they measured by a factor of ~2–3. This difference may be explained by the changes of jet speed and viewing angle or the variability of the emitting region during the flaring or jet bending or core wandering (Niinuma et al. 2015; Hodgson et al. 2017; Lisakov et al. 2017).

5.3. Magnetic Field Strengths

After carefully analyzing the data in Sections 4.5 and 4.6, we found only three epochs could be used to determined the magnetic field strengths. We found that within errors the B_{SSA} did not change. The B_{eq} is slightly lower in the last two epochs but given the assumptions and uncertainties we cannot claim that this trend is significant. However, the difference between B_{SSA} and B_{eq} is an order of magnitude. The assumptions in the equipartition measurements could account for an order of magnitude of difference Longair (1994). However, the difference here is large enough that we are confident in claiming that the source is not in equiparititon. That B_{SSA} is much smaller than B_{eq} suggests that the core is particle dominated, which is consistent with the results of Algaba et al. (2018b).
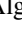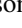
6. Summary

We presented the results of VLBI observations of OJ 287 with the KVN at 22, 43, 86, and 129 GHz and combining the 15 GHz (OVRO) and 225 GHz (SMA) data over ~4 yr from 2013 to 2017. We explored variability, physical parameters of the jet, and spectral variations by analyzing the multifrequency light curves. We draw our conclusions as below.

1. OJ 287 shows compact core-dominated structure on the milliarcsecond scale at 22–129 GHz under the KVN resolutions of 1–6 mas.
2. The source shows several flux density enhancements at 15–225 GHz light curves, which are divided into four parts designated as P1–P4. The timescales of the flux enhancements for P1–P4 are in the range of 49–128 days at 15 GHz and of 48–119 days at 225 GHz.
3. The fractional variability amplitudes in a range of 0.26–0.34 are relatively constant over observing frequencies of 15–86 GHz.
4. The significant correlations between 15 and 225 GHz light curves are found. The flux density variability at high frequency leads that at a low frequency, which can be explained by the opacity effect.
5. The turnover frequency and peak flux density are in the range of 27–50 GHz and 3–6 Jy, respectively.
6. The synchrotron self-absorbed magnetic field strengths are in the range of 0.157 ± 0.104–0.255 ± 0.146 mG and the equipartition magnetic field strengths are in the range of $0.95 \pm 0.240.15$–1.93 ± 0.30 mG. The equipartition magnetic field strength is larger by a factor of 10 than synchrotron self-absorbed magnetic field, indicating that the downstream of the jet may be more particle dominated.

ORCID iDs

Jee Won Lee ⃝ https://orcid.org/0000-0003-2147-0290
Sang-Sung Lee ⃝ https://orcid.org/0000-0002-6269-594X
Juan-Carlos Algaba ⃝ https://orcid.org/0000-0001-6993-1696
Jeffrey Hodgson ⃝ https://orcid.org/0000-0001-6094-9291
Jae-Young Kim ⃝ https://orcid.org/0000-0001-8229-7183
Jongho Park ⃝ https://orcid.org/0000-0001-6558-9053
Motoki Kino ⃝ https://orcid.org/0000-0002-2709-7338
Dae-Won Kim ⃝ https://orcid.org/0000-0003-4997-2153
Sincheol Kang ⃝ https://orcid.org/0000-0002-0112-4836
Sungmin Yoo ⃝ https://orcid.org/0000-0002-2046-4190
Mark Gurwell ⃝ https://orcid.org/0000-0003-0685-3621

References

Agudo, I., Jorstad, S. G., Marscher, A. P., et al. 2011, ApJL, 726, L13
Agudo, I., Marscher, A. P., Jorstad, S. G., et al. 2012, ApJ, 747, 63
Algaba, J.-C., Lee, S.-S., Kim, D.-W., et al. 2018a, ApJ, 852, 30
Algaba, J.-C., Lee, S.-S., Rani, B., et al. 2018b, ApJ, 859, 128
Algaba, J. C., Nakamura, M., Asada, K., et al. 2017, ApJ, 834, 65
Algaba, J.-C., Zhao, G.-Y., Lee, S.-S., et al. 2015, JKAS, 48, 237
Aller, M. F., Aller, H. D., Hughes, P. A., & Latimer, G. E. 1999, ApJ, 512, 601
Angel, J. R. P., & Stockman, H. S. 1980, ARA&A, 18, 321
Begelman, M. C., Blandford, R. D., & Rees, M. J. 1984, RvMP, 56, 255
Blandford, R. D., & Königl, A. 1979, ApJ, 232, 34
Britzen, S., Fendt, C., Witzel, G., et al. 2018, MNRAS, 478, 3199
Chidiac, C., Rani, B., Krichbaum, T. P., et al. 2016, A&A, 590, A61
Deller, A. T., Brisken, W. F., Phillips, C. J., et al. 2011, PASP, 123, 275
Deller, A. T., Tingay, S. J., Bailes, M., & West, C. 2007, PASP, 119, 318
Edelson, R., Turner, T. J., Pounds, K., et al. 2002, ApJ, 568, 610
Edelson, R. A., & Krolik, J. H. 1988, ApJ, 333, 646
Gurwell, M. A., Peck, A. B., Hostler, S. R., Darrah, M. R., & Katz, C. A. 2007, in ASP Conf. Ser. 375, From Z-Machines to ALMA: (Sub)millimeter Spectroscopy of Galaxies, ed. A. J. Baker et al. (San Francisco, CA: ASP), 234
Heeschen, D. S., Krichbaum, T., Schalinski, C. J., & Witzel, A. 1987, AJ, 94, 1493
Hodgson, J., Lee, S.-S., Zhao, G.-Y., et al. 2016, JKAS, 49, 137
Hodgson, J. A., Krichbaum, T. P., Marscher, A. P., et al. 2017, A&A, 597, A80
Jorstad, S. G., Marscher, A. P., Lister, M. L., et al. 2005, AJ, 130, 1418

Jorstad, S. G., Marscher, A. P., Morozova, D. A., et al. 2017, ApJ, 846, 98
Kataoka, J., & Stawarz, Ł. 2005, ApJ, 622, 797
Kellermann, K. I., & Pauliny-Toth, I. I. K. 1969, ApJL, 155, L71
Kim, D.-W., Trippe, S., Lee, S.-S., et al. 2018, MNRAS, 480, 2324
Kraus, A., Krichbaum, T. P., Wegner, R., et al. 2003, A&A, 401, 161
Kudryavtseva, N. A., Gabuzda, D. C., Aller, M. F., & Aller, H. D. 2011, MNRAS, 415, 1631
Lee, J. W., Lee, S.-S., Hodgson, J. A., et al. 2017a, ApJ, 841, 119
Lee, J. W., Lee, S.-S., Kang, S., et al. 2016a, A&A, 592, L10
Lee, J. W., Sohn, B. W., Byun, D.-Y., Lee, J. A., & Kim, S. S. 2017b, A&A, 601, A12
Lee, S.-S., Byun, D.-Y., Oh, C. S., et al. 2015, JKAS, 48, 229
Lee, S.-S., Han, M., Kang, S., et al. 2013, EPJWC, 61, 07007
Lee, S.-S., Wajima, K., Algaba, J.-C., et al. 2016b, ApJS, 227, 8
Lisakov, M. M., Kovalev, Y. Y., Savolainen, T., et al. 2017, MNRAS, 468, 4478
Lobanov, A. P. 2005, arXiv:astroph/0503225
Lobanov, A. P., Krichbaum, T. P., Witzel, A., et al. 2006, PASJ, 58, 253
Longair, M. S. 1994, High Energy Astrophysics. Volume 2. Stars, the Galaxy and the Interstellar Medium (Cambridge: Cambridge Univ. Press)
Marscher, A. P. 1977, ApJ, 216, 244
Marscher, A. P. 1983, ApJ, 264, 296
Max-Moerbeck, W., Richards, J. L., Pavlidou, V., et al. 2012, arXiv:1205.0276
Myserlis, I., Komossa, S., Angelakis, E., et al. 2018, A&A, 619, A88
Niinuma, K., Kino, M., Doi, A., et al. 2015, ApJL, 807, L14
Nilsson, K., Takalo, L. O., Lehto, H. J., & Sillanpää, A. 2010, A&A, 516, A60
Park, J., Lee, S.-S., Kim, J.-Y., et al. 2019, ApJ, 877, 106
Peterson, B. M., Wanders, I., Horne, K., et al. 1998, PASP, 110, 660
Pushkarev, A. B., Hovatta, T., Kovalev, Y. Y., et al. 2012, A&A, 545, A113
Rani, B., Krichbaum, T. P., Fuhrmann, L., et al. 2013, A&A, 552, A11
Richards, J. L., Max-Moerbeck, W., Pavlidou, V., et al. 2011, arXiv:1111.0318
Rybicki, G. B., & Lightman, A. P. 1986, Radiative Processes in Astrophysics (Oxford: Wiley)
Sillanpaa, A., Haarala, S., Valtonen, M. J., Sundelius, B., & Byrd, G. G. 1988, ApJ, 325, 628
Simonetti, J. H., Cordes, J. M., & Heeschen, D. S. 1985, ApJ, 296, 46
Sitko, M. L., & Junkkarinen, V. T. 1985, PASP, 97, 1158
Spergel, D. N., Flauger, R., & Hložek, R. 2015, PhRvD, 91, 023518
Urry, C. M., & Padovani, P. 1995, PASP, 107, 803
Valtonen, M., & Pihajoki, P. 2013, A&A, 557, A28
Valtonen, M. J., Lehto, H. J., Nilsson, K., et al. 2008, Natur, 452, 851
Valtonen, M. J., Lehto, H. J., Sillanpää, A., et al. 2006, ApJ, 646, 36
Villforth, C., Nilsson, K., Heidt, J., et al. 2010, MNRAS, 402, 2087